Catalog of Void Galaxies in the Sloan Digital Sky Survey

Randall R. Rojas, Michael S. Vogeley, and Fiona Hoyle
Department of Physics, Drexel University, 3141 Chestnut Street, Philadelphia, PA 19104

rrojas@mercury.physics.drexel.edu, vogeley@drexel.edu,
hoyle@venus.physics.drexel.edu

ABSTRACT

We present a catalog of more than 10^3 void galaxies from the Sloan Digital Sky Survey. We use a nearest neighbor analysis to construct the sample of void galaxies. The density field of galaxies is traced using a volume-limited sample with $z_{max} = 0.089$. Galaxies from the flux-limited SDSS with $z \leq z_{max}$ and fewer than three volume-limited neighbors within $7h^{-1}$Mpc are classified as void galaxies. Details of how the sample of void galxies is obtained are discussed in Rojas et al. (2003). These galaxies have density contrast $\delta\rho/\rho < -0.6$ and span a range of absolute magnitude from $M_r = -13.5$ to $M_r = -22.5$ with redshift $z < 0.089$. Measured photometric parameters from the SDSS `photo` pipeline include, the absolute magnitude in u, g, r, i, z, concentration index, and Sersic index. In addtion, spectroscopic parameters from the SDSS `spectro1d` pipeline such as the equivalent width, sigma, and height of the fitted Gaussian to the respective line are also included for 5 emission lines. Derived star formation and specific star formation rates from Hα are also included. We provide the 4000 Å Balmer strength and stellar masses from Kauffmann et al. (2003; K03a). For other galaxies in our sample not included in K03a we estimate the stellar masses from a least squares fit using the z-band flux. Color composite images and calibrated spectra of all objects are also available. Rojas et al. (2003, 2004) studied the photometric and spectroscopic properties of these galaxies and discovered that they are bluer, more late-type, have larger emission line equivalent widths, larger specific star formation rates, smaller stellar masses and smaller 4000 Å Balmer break than non-void galaxies of similar luminosities and surface brightness profiles. Hoyle et al. (2003) computed the corresponding luminosity function and found that voids are not filled with a large population of dwarf galaxies. The metallicities of these void galaxies were studied by Hao et al. (2004) and it was found that they have slightly lower metallicities than galaxies in more typical environments.

Subject headings: catalogs – galaxies: large-scale structure of the universe – *On-line material*: machine-readable table

1. Introduction

Since the discovery of the void in Boötes (Kirshner et al. 1981), with a diameter of $50h^{-1}$Mpc, and subsequent discoveries of voids in larger redshift surveys (Geller & Huchra 1989; Pellegrini, da Costa & de Carvalho 1989; da Costa et al. 1994; Shectman et al. 1996; El-Ad, Piran & da Costa 1996, 1997; Müller et al. 2000; Plionis & Basilakos 2002; Hoyle & Vogeley 2002), these structures have posed an observational and theoretical challenge. Because the characteristic scale of large voids was comparable to the depth of early redshift surveys, few independent structures were detected, making statistical analysis of their properties difficult. Likewise, the limitations of computing technology constrained early cosmological simulations to include only a few voids per simulation.

Whether voids are empty or not has been the question of recent debate. Peebles (2001) pointed out the apparent discrepancy between Cold Dark Matter Models (CDM) and observations. CDM models predict mass and hence, maybe galaxies inside the voids, (Dekel & Silk 1986; Hoffman, Silk & Wyse 1992). However, pointed observations toward void regions failed to detect a significant population of faint galaxies (Kuhn, Hopp & Elsässer 1997; Popescu, Hopp & Elsässer 1997; McLin et al. 2002). Surveys of dwarf galaxies indicate that they trace the same overall structures as larger galaxies (Bingelli 1989). Thuan, Gott & Schneider (1987), Babul & Postman (1990) and Mo, McGaugh & Bothun (1994) showed that galaxies had common voids regardless of Hubble type.

Grogin & Geller (1999, 2000) identified a sample of 149 galaxies that lie in voids traced by the Center for Astrophysics Survey. The void galaxies were found in the Century and 15R redshift samples. Grogin & Geller showed that the void galaxies tended to be bluer and that a significant fraction of them were of late type. Their sample of 149 void galaxies covered a narrow range of absolute magnitude ($-20 \lesssim B \lesssim -17$) of which 49 have a low density contrast of $\delta\rho/\rho \leq -0.5$. Our sample of void galaxies is large enough to allow comparison of void and wall galaxies with the same color, surface brightness profile and luminosity to statistically quantify their differences. The range of absolute magnitude (SDSS r-band) in our sample ($-22 \lesssim M_r \lesssim 13$) is large enough to include faint dwarfs to giants.

In this paper, we introduce a new sample of void galaxies from the Sloan Digital Sky Survey (SDSS). The large sky coverage and depth of the SDSS provides us with the opportunity to identify for the first time more than 10^3 void galaxies with $\delta\rho/\rho \leq -0.6$. In Section 2 we discuss the galaxy redshift samples. In Section 3 describe how we find the void galaxies and in Section 4 we present the catalog of void galaxies. Sample images and spectra are presented in Section 5 and a discussion of unusual void galaxies is given in Section 6. Finally in Section 7 we discuss the conclusions.

2. The Redshift Surveys

The search for void galaxies requires a large 3-dimensional map of the galaxy density field. We extract a volume-limited sample from the SDSS data to map the galaxy density field and look for void galaxies in the full magnitude-limited sample. As the SDSS currently has a slice-like geometry, with each slice only $\sim 6^\circ$ thick, large voids of radius $\sim 10h^{-1}$Mpc ($h \equiv H_o/100$km s^{-1}Mpc^{-1}) can only be detected at comoving distances of $r \gtrsim 10^2 h^{-1}$Mpc using the SDSS data alone. Therefore, to trace the local voids, we also extract a volume-limited sample from the combined Updated Zwicky Catalog (UZC; Falco et al. 1999) and Southern Sky Redshift Survey (SSRS2; da Costa et al. 1998). It should be noted that nearby void galaxies are not selected from the UZC and SSRS2 surveys. These surveys are only used to define the density field around SDSS galaxies that lie at distances $r \leq 72h^{-1}$Mpc. These surveys are described in more detail below.

2.1. The SDSS

Observations for the SDSS are taken using a dedicated 2.5 m telescope, located at Apache Point Observatory (APO) in New Mexico, with a 3° field of view. The telescope has two instruments: a CCD imaging camera that takes data in drift-scanning mode, nearly simultaneously in five photometric bands, u, g, r, i, and z, and a pair of double spectrographs that use fiber optics to simultaneously take spectra of 640 objects selected from the imaging data. The imaging data are taken on nights of pristine conditions (photometric, good seeing, no Moon), while spectroscopy is done on those nights that are less than perfect. The data are photometrically calibrated with the aid of an auxiliary 20 inch (0.5 m) telescope, the photometric telescope (PT), at the site. The data are processed through a series of interlocking pipelines that find the objects in the imaging data, measure their properties, apply astrometric and photometric calibrations, select objects for spectroscopic follow-up, extract and calibrate the spectra, and derive redshifts and spectral types from the spectra.

The completed survey will cover approximately 10^4 square degrees. CCD imaging of 10^8 galaxies in five colors and follow-up spectroscopy of 10^6 galaxies with $r < 17.77$ will be obtained. York et al. (2000) provides an overview of the SDSS and Stoughton et al. (2002) describes the early data release (EDR) and details about the photometric and spectroscopic measurements made from the data. Abazajian et al. (2003) describes the First Data Release (DR1) of the SDSS. Technical articles providing details of the SDSS include descriptions of the photometric camera (Gunn 1998), photometric analysis (Lupton et al. 2002), the photometric system (Fukugita et al. 1996; Smith et al. 2002), the photometric monitor (Hogg et al. 2001), astrometric calibration (Pier et al. 2002), selection of the galaxy spectroscopic samples (Strauss et al. 2002; Eisenstein et al. 2001), and spectroscopic tiling (Blanton et al. 2001). A thorough analysis of possible systematic uncertainties in the galaxy samples is described in Scranton et al. (2002).

We examine a sample of 155,126 SDSS galaxies (Blanton et al. 2002; `sample10`) that have both

completed imaging and spectroscopy. To a good approximation, the sample we analyze consists of roughly three regions covering a total angular area of 1,986 deg^2. The area observed by `sample10` is approximately 1.5 times that of the DR1 (Abazajian et al. 2003). Due to the complicated geometry of the SDSS sky coverage, the survey regions are best described in the SDSS coordinate system (see Stoughton et al. 2002). Where possible in this section we describe approximate limits in the more familiar equatorial coordinates. The first region is an equatorial stripe in the North Galactic Cap (NGC). This stripe has a maximum extent of 7.5° in the declination direction over the R.A. range $21^{\rm h}30^{\rm m} \lesssim \alpha \lesssim 4^{\rm h}10^{\rm m}$ and maximum length of 120° over the R.A. range $8^{\rm h} \lesssim \alpha \lesssim 16^{\rm h}$. The second region is in the South Galactic Cap (SGC). There are three stripes, the boundaries of which are defined in the SDSS coordinate system. Each stripe is 2.5° wide in SDSS survey coordinates. One stripe is centered at $\delta = 0°$ and covers the R.A. range $20^{\rm h}40^{\rm m} \lesssim \alpha \lesssim 2^{\rm h}20^{\rm m}$. The other two stripes are above and below the equator and cover similar R.A. ranges. In survey coordinates these two stripes cover the range $-28° \lesssim \lambda \lesssim 41°$, $130° \lesssim \eta \lesssim 135°$ and $-57° \lesssim \lambda \lesssim 58°$, $155° \lesssim \eta \lesssim 160°$. The third large region is in the North Galactic Cap. In SDSS survey coordinates it covers the range $-48° \lesssim \lambda \lesssim 50°$, $75° \lesssim \eta \lesssim 85°$. There are additional smaller stripes at $-37° \lesssim \lambda \lesssim -22°$, $60° \lesssim \eta \lesssim 70°$ and $2° \lesssim \lambda \lesssim 60°$, $90° \lesssim \eta \lesssim 100°$ (the boundary is an approximation because of the tiling geometry).

We correct the velocities of galaxies to the Local Group frame according to

$$\Delta v = V_{\rm apex}[\sin(b)\sin(b_{\rm apex}) + \cos(b)\cos(b_{\rm apex})\cos(l - l_{\rm apex})] \quad (1)$$

where $l_{\rm apex} = 93°$, $b_{\rm apex} = -4°$, and $V_{\rm apex} = 316\,{\rm km\,s^{-1}}$ (Karachentsev & Makarov 1996). The magnitudes of the galaxies are K-corrected as described in Blanton et al. (2003) and corrections for Galactic extinction are made using the Schlegel, Finkbeiner, & Davis (1998) dust maps. Finally, to convert redshifts into comoving distances we adopt an $(\Omega_{\rm m}, \Omega_\Lambda) = (0.3, 0.7)$ cosmology.

The decrease of observed galaxy density with distance in an apparent magnitude-limited galaxy sample might cause us to erroneously detect more voids at large distances. Therefore, we use a volume-limited sub-sample of the SDSS to define the density field of galaxies. This sample consists of galaxies with redshifts less than the redshift limit, z_{max}, and SDSS r-band absolute magnitudes brighter than $M_{\rm crit}$, where

$$M_{\rm crit} = r_{\rm lim} - 25 - 5{\rm log}_{10}[d_l({\rm z_{max}})] \quad (2)$$

$r_{\rm lim}$[1], is the magnitude limit of the survey and d_l, is the luminosity distance in units of h^{-1}Mpc at $\rm z_{max}$. We form a volume-limited sample of the SDSS with $\rm z_{max} = 0.089$, with corresponding absolute-magnitude limit $M_{\rm crit} = -19.87$ (in the SDSS r-band). The redshift limit $\rm z_{max} = 0.089$ allows us to construct the largest possible volume-limited sample from the current SDSS sample. This volume-limited sample contains 22,866 galaxies where the mean separation between these galaxies is $\sim 5.3h^{-1}$Mpc. For a $(\Omega_{\rm m} = 0.3, \Omega_\Lambda = 0.7)$ cosmology, the redshift limit of $z_{\rm max}$=0.089,

[1]We use $r_{\rm lim} = 17.5$ instead of $r_{\rm lim} = 17.77$, in the construction of volume-limited catalog to ensure we have a uniform limit across all the data since earlier stripes were only observed to $r_{\rm lim} = 17.5$.

corresponds to a comoving distance of $260h^{-1}$Mpc. The lower bound of $100h^{-1}$Mpc on the comoving distance is necessary due to the slice-like geometry of the early SDSS slices. Recall that voids of radii $\gtrsim 10h^{-1}$Mpc can only be found at $r \gtrsim 100h^{-1}$Mpc as discussed in Section 2.

2.2. The Updated Zwicky Catalog

The Updated Zwicky Catalog (Falco et al. 1999) includes a re-analysis of data taken from the Zwicky Catalog and Center for Astrophysics surveys (Zwicky et al. 1961-1968; Geller & Huchra 1989; Huchra et al. 1990; Huchra, Geller, & Corwin 1995; Huchra, Vogeley, & Geller 1999) together with new spectroscopic redshifts for some galaxies and coordinates from the digitized POSS-II plates. Improvements over the previous catalogs include estimates of the accuracy of the CfA redshifts and uniformly accurate coordinates at the $< 2''$ level.

The UZC contains 19,369 galaxies. Of the objects with limiting apparent magnitude $m_{\rm Zw} \leq 15.5$, 96% have measured redshifts, giving a total number of 18,633 objects. The catalog covers two main survey regions: $8^h < \alpha_{1950} < 17^h, 8.5^\circ < \delta_{1950} < 44.5^\circ$ in the North Galactic Cap and $20^h < \alpha_{1950} < 4^h, -2.5^\circ < \delta_{1950} < 48^\circ$ in the South Galactic Cap. We correct the velocities of the galaxies with respect to the Local Group as discussed in Section 2.1. The magnitudes of the galaxies are corrected for Galactic extinction using the Schlegel, Finkbeiner & Davis (1998) dust maps and the magnitudes are K-corrected assuming $K = 3$, which is appropriate for the B filter and the median galaxy morphological type Sab (Park et al. 1994; Pence 1976; Efstathiou, Ellis & Peterson 1988).

We construct a volume-limited UZC sample with $\rm z_{max} = 0.025$ since this is the redshift at which the largest volume-limited sample can be obtained. This volume-limited sample contains 4924 galaxies, has a co-moving depth of $\sim 76h^{-1}$Mpc and absolute-magnitude limit of $M_{lim} \leq -18.96$ ($B_{\rm Zw}$). To compare this limit to that of the SDSS, we translate a B-band magnitude into an approximate r-band magnitude of $M_r = -20.06$ using $g - r = 0.66$ and $g - B = -0.45$ from Fukugita et al. (1995). The absolute magnitude limit of the UZC sample is therefore, slightly brighter than the SDSS limit. To ensure that this sample and the SSRS2 described below are equally deep, we cut back this sample to $72h^{-1}$Mpc.

2.3. The SSRS2

The SSRS2 galaxy sample (da Costa et al. 1998) was selected from the list of nonstellar objects in the Hubble Space Telescope Guide Star Catalog (GSC). The SSRS2 contains 3489 galaxies in the SGC over the angular region: $\delta_{1950} \leq -2.5^\circ$ and $b \leq -40^\circ$, covering a total of 1.13 sr with $m_{\rm SSRS2} \leq 15.5$, where the zero-point offset from the Zwicky magnitude system used in the UZC is approximately $m_{\rm SSRS2} - m_{\rm Zwicky} \sim 0.10$ mag (Alonso et al. 1994).

We construct a volume-limited sample with the same redshift limit as for the UZC, $z_{max} = 0.025$ (same reason as discussed in Section 2.2) and (after adjustment of the zeropoint), $M \leq -18.96$. For our chosen cosmology, the depth of the sample is $\sim 73h^{-1}$Mpc which we also cut back to $72h^{-1}$Mpc as discussed in the case for the UZC sample. Therefore, both SSRS2 and UZC volume-limited samples have the same co-moving depth.

As above (Section 2.1), we correct galaxy velocities to the Local Group frame, apply the Galactic dust corrections based on the Schlegel, Finkbeiner, & Davis (1998) dust maps, and assume $K = 3$ to K-correct the observed magnitudes. This volume-limited sample includes 725 galaxies.

The SSRS2 provides angular coverage in the South Galactic Cap. The combined UZC+SSRS2 sample contains 5649 galaxies and sky coverage of $\sim 4.25\,\mathrm{sr}$.

2.4. Summary of Surveys

To recap, we have two volume-limited samples, one from the SDSS and one from the combined UZC+SSRS2. These samples are used to define the galaxy density field only. Void galaxies are found from the magnitude-limited SDSS sample. We define the Distant sample to be the SDSS magnitude-limited sample truncated at $100 \leq r \leq 260h^{-1}$Mpc. The Nearby sample is the SDSS magnitude-limited sample truncated at $r = 72h^{-1}$Mpc. Both magnitude-limited samples (Nearby and Distant) are constructed using the SDSS r-band. In this section we describe each of the surveys and samples in detail.

The left hand plot of Figure 1, shows an Aitoff projection of the three surveys. The black points show the SDSS galaxies and the gray dots show the UZC+SSRS2 galaxies. This figure demonstrates that in terms of area, the SDSS is almost totally embedded in the UZC+SSRS2 data apart from along the bottom edge of the northern equatorial slice and a small part of the southern most slice. Therefore, the combined UZC+SSRS2 survey is useful for defining the large-scale galaxy density field around the SDSS sample out to a distance of approximately $72h^{-1}$Mpc.

The right-hand plot in Figure 1 shows a cone diagram of the SDSS data with $|\delta| \lesssim 15°$. The inner circle is drawn at $72h^{-1}$Mpc, which is the co-moving depth of the combined UZC and SSRS2 volume-limited sample. The outer circle is drawn at $260h^{-1}$Mpc, which is the co-moving depth of the SDSS volume-limited sample. Beyond $72h^{-1}$Mpc, the selection function (number of observed galaxy density with distance) of these shallower surveys drops and the thickness (in the declination direction) of the SDSS itself is adequate to define the density field around the SDSS galaxies.

3. Identifying Void Galaxies Using Nearest Neighbor Statistics

We search for void galaxies in the SDSS using the nearest neighbor statistic. The two volume limited samples (SDSS and UZC+SSRS2) are used to trace the voids. Any magnitude-limited

galaxy that lies away from the boundary of the volume-limited sample and has less than 3 volume-limited sample neighbors in a sphere of $7h^{-1}$Mpc is considered a void galaxy. We expand on each of these steps below.

3.1. Proximity to Survey Boundary

Galaxies in the magnitude-limited SDSS samples that lie near the boundaries of the volume-limited samples have systematically larger distances to their third nearest neighbors than galaxies that lie deep in the volume-limited samples. This is because potentially closer neighbors have not been observed/included in the sample. These galaxies have a higher probability of being selected as void galaxies than the galaxies inside the survey. We correct for this bias in the following way: We generate a random catalog with the same angular and distance limits as the corresponding volume-limited sample (SDSS and UZC+SSRS2) but with no clustering. We count how many random points lie around each of the magnitude-limited SDSS galaxies. If the density around a galaxy is less than a certain value, we reject it from the SDSS samples. This is explained further below.

To remove galaxies near the boundary of the survey we:

- go to a galaxy from the magnitude-limited sample
- count how many random points (N) lie in a sphere of size, $r = 3.5h^{-1}$Mpc around this galaxy
- compute the respective number density, $\rho = N/V$, where, $V = (\frac{4\pi}{3}r^3)$
- we know the expected number density in the random sample ($\rho_{random} = N_{random}/\frac{\Omega}{3}r^3$)
- if $\rho < \rho_{\rm random}$, remove this galaxy from the magnitude-limited sample (its proximity to the sample's boundaries causes $\rho < \rho_{\rm random}$)
- repeat steps above until every magnitude-limited galaxy has been tested.

We apply this procedure twice, once when we compare the distant SDSS magnitude-limited sample with the SDSS random catalog and again when we compare the nearby SDSS magnitude-limited sample with the UZC+SSRS2 random catalog. The distant SDSS sample is reduced from 65,186 galaxies to 13,742 galaxies, the nearby SDSS sample is reduced from 3784 galaxies to 2,450 galaxies. The nearby SDSS sample is cut less drastically as the UZC+SSRS2 sample covers a greater area.

Because the SDSS is not finished, the angular selection function is complicated (see Figure 1). An algorithm to quantify the fraction of galaxies that have been observed in any given region, i.e. the completeness, has been developed and is described in Tegmark, Hamilton, & Xu (2002). The completeness for any given (α, δ) coordinate is returned, allowing a random catalog with the

same angular selection function to be created. For the SDSS, the completeness within the regions that have been observed is typically $> 90\%$. The angular selection function for the combined UZC+SSRS2 sample is easier as the surveys are finished and the completeness for the UZC is $\sim 96\%$.

3.2. Nearest Neighbor

We identify galaxies with a large distance to their *nth* nearest neighbor as void galaxies. We follow the work of El-Ad & Piran (1997) and Hoyle & Vogeley (2002) and use $n = 3$ rather than $n = 1$ in the nearest neighbor analysis. It is a fact that galaxies cluster, therefore, it is not unreasonable to expect that void galaxies might also be found in small groups. If we used $n = 1$ then a pair of galaxies in an otherwise low density environment would not be classified as void galaxies, hence we set $n = 3$. Note that we do not make any corrections for peculiar velocities along the line of sight. Therefore, we might underestimate the density of systems with large velocity dispersions which could pollute the void galaxy population. This could lead to a slight underestimate of the differences between the void and wall populations.

We find the third nearest neighbor distance for each galaxy in the SDSS magnitude-limited samples to galaxies from the corresponding volume-limited samples, then compute the average separation distance $\bar{d}^{(3)}_{sep}$ and the standard deviation, $\sigma^{(3)}_{sep}$ of this distance. We fix the search radius $d_{\rm crit}$ to be $7h^{-1}$Mpc which is approximately equal to $\bar{d}^{(3)}_{sep}+1.5\sigma^{(3)}_{sep}$ found from the two samples, (the actual values are given in Sections 3.3 and 3.4). This also agrees with the criterion for defining wall and void galaxies in `VOIDFINDER` (Hoyle & Vogeley 2002). Galaxies that have their third nearest neighbor at a distance $\geq d_{\rm crit} = 7h^{-1}$Mpc are classified as void galaxies. The galaxies that we classify as void galaxies are then removed from the parent SDSS sample. This yields two mutually exclusive catalogs which we will refer to from now on as void and wall galaxies. To test for possible bias in the redshift distribution of void and wall galaxies, we construct ten mock volume and flux-limited samples with geometry identical to the SDSS survey, using mock galaxies drawn from the Virgo Consortium's Hubble Volume z=0 ΛCDM simulation (Frenk et al. 2000). This test confirms that our procedure for identifying void galaxies and removing objects (both void and wall) near the survey boundaries does not produce any bias in the redshift distribution of void and wall galaxies.

To test that our procedure has identified genuine void galaxies, we compute the mean, median and upper bound of the density contrast ($\delta\rho/\rho$) around void galaxies and compare these values to the emptiness of voids as defined by `VOIDFINDER`. The number of galaxies in the SDSS volume-limited sample is 22,866 and the respective volume, $V = \frac{\Omega}{3}(r^3 - r_o^3) = \frac{0.6}{3}(260^3 - 100^3) = 3.32\times10^6 h^{-3}\mathrm{Mpc}^3$, therefore, the mean density is $\bar{\rho} = 6.84 \times 10^{-3} h^3\mathrm{Mpc}^{-3}$. The void galaxies contain less than three neighbors in a sphere of $7h^{-1}$Mpc, thus, the density around the void galaxies is $\rho_v \leq 4/(\frac{4\pi}{3})7^3 = 2.78 \times 10^{-3} h^3\mathrm{Mpc}^{-3}$. Therefore, the density contrast around void galaxies in the distant sample is $(\rho_v - \bar{\rho})/\bar{\rho} \leq -0.6$. This number is very similar for the nearby sample. It is an upper bound, as the median third nearest neighbor distance to the void galaxies is closer to $8h^{-1}$Mpc, giving

values for the density contrast closer to $\delta\rho/\rho = -0.8$. This value is low, although not as low as that found by VOIDFINDER for the density contrast of the voids. Since we are centered on a galaxy and galaxies are clustered, we expect the density around void galaxies (ρ_{vg}) to be higher than the mean density of a void ($\bar{\rho}_{void}$). Recall that the mean density of a void is about 0.1× mean density of the universe ($\bar{\rho}_{universe}$) and since the correlation length (ξ) on spheres of $8h^{-1}$Mpc is ~ 1 ($\sigma_8 \sim 1$), then: $\rho_{vg}(r \leq 7h^{-1}\mathrm{Mpc}) = \bar{\rho}_{void} \times (1 + \xi(r = 7h^{-1}\mathrm{Mpc})) \sim 2 \times \bar{\rho}_{void}$. In addition, void galaxies are typically found near the the edge of the void where the density is higher.

It is important to keep in mind that since most of the void galaxies will lie near the edges of voids, the typical density contrast around void galaxies is less extreme than the density contrast of the whole void region (see Figure 11 in Benson et al. 2003). The average number of volume-limited galaxies in a sphere of radius $7h^{-1}$Mpc around a wall galaxy is 25 compared to 2 around a void galaxy, demonstrating that void galaxies really are in highly underdense regions.

3.3. Distant Void Galaxies

For SDSS galaxies that lie in the distant SDSS sample, we use the SDSS volume-limited sample to define the galaxy density field. Using the third nearest neighbor ($n = 3$), we obtain $(\bar{d}^{(3)}_{sep}, \sigma^{(3)}_{sep}) = (3.6, 2.10)h^{-1}$Mpc, from which we obtain $d_{\mathrm{crit}} = 6.75h^{-1}$Mpc, which we round up to $7h^{-1}$Mpc. From the distant SDSS sample of 13,742 galaxies we find 1010 void galaxies. This sample of void galaxies will be referred to as VGD (as in Void Galaxy Distant). The sample of 12,732 non-void galaxies we label WGD (as in Wall Galaxy Distant). The fraction of void galaxies in the distant sample is $\sim 8\%$. This is only slightly higher than the fraction of void galaxies found by VOIDFINDER (Hoyle & Vogeley 2002) and by El-Ad & Piran (1997).

Figure 2 shows a redshift cone diagram of the SDSS volume-limited galaxies (gray dots) and the corresponding void galaxies, VGD (black points). We plot only galaxies with $|\delta| \lesssim 15°$. Note that some of the void galaxies appear to be close to volume-limited galaxies. This is merely a projection effect. All the void galaxies have less than three neighbors within a radius of $7h^{-1}$Mpc.

3.4. Nearby Void Galaxies

To find faint void galaxies, which are present only at small comoving distances, we use the UZC+SSRS2 volume-limited sample to trace the voids because the slice-like SDSS samples are too thin to detect three-dimensional voids in this nearby volume.

The number of galaxies in the SDSS nearby sample, after applying the boundary corrections, is 2456. We measure the distance to the third nearest UZC+SSRS2 volume-limited galaxy and obtain the values $(\bar{d}^{(3)}_{sep}, \sigma^{(3)}_{sep}) = (3.9, 1.9)h^{-1}$Mpc, hence the choice of $d_{\mathrm{crit}} = 7h^{-1}$Mpc is still applicable. In this case we find 194 void galaxies. We refer to this void galaxy sample as VGN (N for nearby)

and the respective parent wall galaxy sample (after removing the respective void galaxies) as WGN.

4. The Void Galaxy Catalog

Here we provide the list of parameters that are included in the two (nearby and distant) catalogs of void galaxies. A brief description of each parameter is included next to each entry in Table 1. and a more detailed discussion is given in the following sections. Both catalogs (nearby and distant) have the same number of columns and parameters as those listed in Table 1. There are 1010 void galaxies in the distant sample and 194 and the nearby sample.

4.1. The SDSS Coordinate System

RA and DEC

Details of the SDSS coordinate system are given in Stoughton et al. (2002), however, we provide a brief review below. The SDSS coordinate system (λ, η) consists of a spherical coordinate system with poles at $\alpha = 95°$, $\delta = 0°$ and $\alpha = 275°$, $\delta = 0°$ (J2000). Where α and δ are the RA and DEC in J2000 Equatorial coordinates respectively.

The survey equator is a great circle perpendicular to the J2000 celestial equator, intersecting it at $\alpha = 185°$ and $\alpha = 5°$. Lines of constant η are great circles perpendicular to the survey equator, and lines of constant λ are small circles parallel to the survey equator; $\lambda = 0°$, $\eta = 0°$ is located at $\alpha = 185°$, $\delta = 32.5°$, with η increasing northward.

The survey area is divided into stripes, where each stripe is centered along a line of constant η, separated from the adjoining stripe or stripes by 2.5°. Each drift scan tracks a survey stripe, offset by $\pm 386''$ perpendicular to the stripe. Two scans (or "strips"), one offset to the north and one to the south, are required to fill a stripe. The survey latitude tracked by stripe n is given by

$$\eta = (\eta - 10) \times 2.5° - 32°.5 \tag{3}$$

in the northern Galactic hemisphere, and by

$$\eta = (\eta - 82) \times 2.5° - 32.5° \tag{4}$$

for the three stripes in the southern Galactic hemisphere. These stripes are superposed on a Galactic extinction map in Figure 2 of York et al. (2000).

The natural coordinate system to use for processing a given drift scan is the *great-circle coordinate system* for that stripe, (μ, ν), in which the equator of the coordinate system is the great circle tracked by the scan. This great circle is inclined by $i = \eta + 32.5°$ to the J2000 celestial equator,

with an ascending node of 95°; $\mu = \alpha$ at the ascending node, and μ increases in the scan direction (east) and ν increases to the north. Each stripe has its own great-circle coordinate system.

The transformation equations between the different coordinate systems are

$$\begin{aligned}
\cos(\alpha - 95^\circ)\cos\delta &= -\sin\lambda & (5)\\
&= \cos(\mu - 95^\circ)\cos\nu, & (6)\\
\sin(\alpha - 95^\circ)\cos\delta &= \cos\lambda\cos(\eta + 32^\circ.5) & (7)\\
&= \sin(\mu - 95^\circ)\cos\nu\cos i - \sin\nu\sin i, & (8)\\
\sin\delta &= \cos\lambda\sin(\eta + +32^\circ.5) & (9)\\
&= \sin\nu\cos i + \sin(\mu - 95^\circ)\cos\nu\sin i & (10)
\end{aligned}$$

Positions of the galaxies are given in right ascension (RA) and declination (DEC) and distances (in comoving coordinates) to the third nearest neighbor are computed using an $(\Omega_m, \Omega_\Lambda) = (0.3, 0.7)$ cosmology with $H_o \equiv 100h\,\mathrm{km\ s^{-1}\,Mpc^{-1}}$.

4.2. SDSS Identification Parameters

Photometric ID Parameters

The run number is a term used to describe one continuous scan of the SDSS imaging camera on the sky, and a stripe is the great circle covered by two runs, 2°.5 wide. Each stripe is covered in two strips, separated in the north-south direction so that the interleaved scans of the six columns of the imaging camera completely cover the stripe. Runs are combined into chunks, contiguous areas of the sky in which spectroscopic targets will be selected and spectroscopic tiling (the process by which targets are assigned to spectroscopic plates) will be done. A segment is a single piece of a run for a single camera column. The frames pipeline (`frames`) detects, deblends, and measures objects, carrying out this processing on a field-by-field basis. Each object detected during the frames analysis of a particular set of data is given a unique identifier, which consists of five integers:

- `run`: A run number refers to a given uninterrupted drift scan.
- `rerun`: Each time we analyze a run with a different set of pipeline versions or calibrations, we assign it a new rerun number. The same rerun number in different runs does not necessarily refer to the same version of the pipelines.
- `camcol`: This number, from 1 to 6, refers to the dewar, or column of photometric CCDs in the imaging camera, with which this object was imaged.

- `fieldID`: This refers to which field the object is in.
- `objID`: This is an identification number for the object that is unique within each field.

Spectroscopic ID Parameters

Plate is the plate number (four digits, zero-padded), MJD is the Modified Julian Day on which observations were completed, and fiber is the fiber of plug plate fiber number (three digits, zero-padded).

4.3. Photometric Parameters

Magnitudes: M_u, M_g, M_r, M_i, M_z

The five SDSS color bands have been chosen to cover from the UV atmospheric cutoff near 3000 Å up to the sensitivity limit for silicon CCDs near 11000 Å. The 5 photometric bands are: u, g, r, i, and z, have design effective wavelengths of 3550, 4770, 6230, 7620, and 9130 Å, respectively (Fukugita et al. 1996; Gunn et al. 1998).

The SDSS has adopted a modified form of the Petrosian (1976) system, measuring galaxy fluxes within a circular aperture whose radius is defined by the shape of the azimuthally averaged light profile.

The "Petrosian ratio" R_P at a radius r from the center of an object is defined as the ratio of the local surface brightness in an annulus at r to the mean surface brightness within r, as described by Blanton et al. 2001a, Yasuda et al. 2001, Strauss et al. 2001:

$$R_P \equiv \frac{\int_{0.8r}^{1.25r} dr' 2\pi r' I(r') / [\pi(1.25^2 - 0.8^2) r^2]}{\int_0^r dr' 2\pi r' I(r') / (\pi r^2)} \tag{11}$$

where $I(r)$ is the azimuthally averaged surface brightness profile.

The Petrosian radius r_P is defined as the radius at which $R_P(r_P)$ equals some specified value $R_{P,lim}$ set to 0.2 in our case. The Petrosian flux in any band is then defined as the flux within a certain number N_P (equal to 2.0 in our case) of r Petrosian radii:

$$F_P = \int_0^{N_P r_P} 2\pi r' I(r') dr' \tag{12}$$

In the SDSS five-band photometry, the aperture in all bands is set by the profile of the galaxy in the r band alone. This procedure ensures that the color measured by comparing the Petrosian flux FP in different bands is measured through a consistent aperture.

Concentration Index

To compare morphological properties of void and wall galaxies, we examine the distribution of concentration indices measured by the SDSS photometric pipeline (Lupton et al. 2001; Stoughton et al. 2002; Pier et al. 2002; Lupton et al. 2002). The concentration index (CI) is defined by the ratio CI $\equiv$ r90/r50, where $r90$ and $r50$ correspond to the radii at which the integrated fluxes are equal to 90% and 50% of the Petrosian flux, respectively. A large value of CI corresponds to a relatively diffuse galaxy and a small value of CI to a highly concentrated galaxy. The concentration index has been shown to correlate well with galaxy type (Strateva et al. 2001; Shimasaku et al. 2001). Spiral galaxies are usually found to have small concentration indices ($\lesssim 2.5$) whereas ellipticals have larger concentration indices ($\gtrsim 2.5$). This bimodal behavior of the concentration index can be clearly seen in Strateva et al. (2001; see Figure 8).

Sersic Index

As another measure of morphology of void and wall galaxies we examine the Sersic index (Sersic 1968), found by fitting the functional form

$$I(r) = A \exp[-(r/r_o)^{1/n}], \tag{13}$$

where n is the Sersic index itself, to each galaxy surface brightness profile (SBP). With this form, $n = 1$ corresponds to a purely exponential profile, while $n = 4$ is a de Vaucouleurs profile. We use the Sersic indices as measured by Blanton et al. (2002) for the SDSS galaxies.

In brief, Blanton et al. (2002) find the parameters A, r_o, and n in equation (13) that minimize χ^2 with respect to the observed i-band radial profile and errors (as expressed by the `profMean` and `profErr` parameters in the SDSS catalog). Sersic profiles have been fitted to the profiles of the other bands as well; the results of the g, r, i, and z profiles are all fairly consistent with one another, while the u-band profile fits tend to be much less concentrated than the others.

4.4. Spectroscopic Parameters

Details of the spectroscopic system are discussed in York et al. (2000). Below we describe the overall features of the spectroscopic system and include a brief discussion on the spectroscopic parameters meaured. The SDSS spectroscopic pipeline uses two spectrographs, each producing 320 spectra. There are thus four CCD detectors, each of the same kind as are present in the g, r, and i bands in the camera, 2048 pixels square with 24 μm pixels. 640 individual spectra observed over a 3°-diameter field at a resolution $R \equiv \lambda/\delta\lambda$ of about 1800 in the wavelength range of 3800-9200 Å. This wavelength range is divided between two cameras by a dichroic at $\sim$ 6150 Å.

For each plate the exposure time is 45 minutes, split into at least three parts for cosmic-ray rejection. 15 minute exposures are repeated until the cumulative median $(\mathrm{S/N})^2 > 15$ at $g^* = 20.2$ and $i^* = 19.9$ in all four cameras. The set of science exposures is preceded and followed by a series

of shorter exposures for calibration: arcs, flat fields, and a 4 minute *smear* exposure on the sky for spectrophotometric calibration, in which the telescope is moved so that the 3″; fiber on each object effectively covers a $5'' \times 8''$ aperture, aligned with the parallactic angle. The smear exposures allows recovery of object light excluded from the 3″ fibers because of seeing and atmospheric refraction; they provide an accurate (albeit low signal-to-noise ratio) measure of the true spectral shape of the objects and are used for spectrophotometric calibration. The calibration and science exposures are immediately processed through a streamlined version of the second spectroscopic pipeline to inform the observers whether the calibrations were successful and to provide signal-to-noise ratio (S/N) diagnostics on the science exposures.

Emission Line Parameters

The spectro1d pipeline analyzes the combined, merged spectra output by spectro2d and determines object classifications (galaxy, quasar, star, or unknown) and redshifts; it also provides various line measurements and warning flags. The code attempts to measure an emission and absorption redshift independently for every targeted (nonsky) object. That is, to avoid biases, the absorption and emission codes operate independently, and they both operate independently of any target selection information.

Emission lines (peaks in the one-dimensional spectrum) are found by carrying out a wavelet transform of the continuum-subtracted spectrum $f_c(\lambda)$:

$$w(a,b) = \frac{1}{\sqrt{b}} \int_{-\infty}^{+\infty} f_c(\lambda) \bar{g} \left(\frac{\lambda - a}{b} \right) d\lambda, \tag{14}$$

where $g(x; a, b)$ is the wavelet (with complex conjugate $\bar{g}$) with translation and scale parameters a and b. The à trous wavelet (Starck, Siebenmorgen, & Gredel 1997) is applied. For fixed wavelet scale b, the wavelet transform is computed at each pixel center a; the scale b is then increased in geometric steps and the process repeated. Once the full wavelet transform is computed, the code finds peaks above a threshold and eliminates multiple detections (at different b) of a given line by searching nearby pixels. The output of this routine is a set of positions of candidate emission lines.

Each significant peak found by the wavelet routine is assigned a trial line identification from the common list (e.g., MgII) and an associated trial redshift. The peak is fitted with a Gaussian, and the line center, width, and height above the continuum are stored in the SpecLine class as parameters wave, sigma, and height, respectively. If the code detects close neighboring lines, it fits them with multiple Gaussians. Depending on the trial line identification, the line width it tries to fit is physically constrained. The code then searches for the other expected common emission lines at the appropriate wavelengths for that trial redshift and computes a confidence level (CL) by summing over the weights of the found lines and dividing by the summed weights of the expected lines. The CL is penalized if the different line centers do not quite match. Once all of the trial line identifications and redshifts have been explored, an emission-line redshift is chosen as the one with the highest CL and stored as z in the EmissionRedshift class. The exact expression for the emission-

line CL has been tweaked to match our empirical success rate in assigning correct emission-line redshifts, based on manual inspection of a large number of spectra from the EDR.

In the catalog we include the height, sigma and equivalent width for Hα, [OII] λ3727, Hβ, [NII] λ6583, and [OIII] λ5007 emission lines. We only provide these 5 emission lines since they are the strongest and any other line can be readily obtained from the SDSS database.

Star Formation Rates

Star formation rates are obtained using Kennicutt's (1998b) prescription for the Hα flux valid in the Case B recombination (Osterbrock 1986) with a Salpeter (1955) initial mass function from

$$\mathrm{SFR} = 7.9 \times 10^{-42} L\,[M_{\odot}\ yr^{-1}], \tag{15}$$

where D_L is the luminosity distance in units of [cm].

Detailed discussions of the Hα derived SFRs can be found in Rojas et al. (2004) and excellent discussions of systematics can be found in Percy et al. (2002), Hopkins et al. (2003) and, Rojas et al. (2004).

Stellar Masses

The integrated stellar masses for our samples are obtained from two sources: the primary source is from K03a's library of stellar masses and the secondary source uses a least squares fit to the stellar mass vs. z-band absolute magnitude relation. The z-band absolute magnitude is our preferred galaxy luminosity measure because it is less affected by extinction and less dependent on stellar age than the other four SDSS bands (u, g, r, i; Fukugita et al. 1996). The reason for obtaining the masses from two different sources is because K03a's library of stellar masses only includes a subset of DR1 (Abazajian 2003) and our samples are from a larger database (Blanton et al. 2002; `sample10`). Therefore, for galaxies in our samples that are missing in K03a's list we need an alternate method to estimate the masses. Given that there is a nearly linear relationship between the z-band absolute magnitude and the logarithm of the estimated stellar mass, a least squares fit ($\mathrm{Log_{10}(mass/M_{\odot}) = -0.5134 M_z - 0.01581}$) is a reasonable approach. Using this fit we can measure typical stellar masses to within a factor of 10.

Specific Star Formation Rates

We estimate the star formation rates per unit stellar mass using the stellar masses from K03a and the absorption, aperture, and dust corrected SFRs as discussed in Rojas et al (2004).

Dn4000

We obtain the strength of the 4000Å Balmer break forthe void galaxies from K03a. K03a's measurements of this index inlcude about 70% of our galaxies. The $\mathrm{D}_n(4000)$ is an excellent spectral indicator of past star formation on timescales of $t \sim 1$Gyr and is also highly insensitive to dust attenuation effects. For hot stars where elements are multiply ionized the opacity decreases,

therefore, hot, young stars (e.g., O and B) have lower amplitudes of $D_n(4000)$ than cooler, older stars (e.g., K and M; see Figure 3, Bruzual 1983). Since late-type galaxies are mainly composed of young stars, their 4000 Å break is smaller than for early-type galaxies which are primarily composed of older stellar populations.

5. Images and Spectra

In Figure 6 we show a small sample of distant and nearby void galaxy images and spectra to show the quality of the observations and a few prominent spectral features. The images are color composites of 5 void galaxies of different morphologies and colors. The complete list of images and spectra can be downloaded from http://www.physics.drexel.edu/SDSS/void_gals.

6. Unusual Void Galaxies

In our sample of void galaxies we find that several of them have unusually high [OIII]/Hβ and [NII]/Hα flux ratios and hence high nuclear activity. Therefore, it prompts the question of whether these galaxies have an Active Galactic Nucleus (AGN)? Void galaxies that have an AGN are not that common, however, given our large sample of void galaxies we find that about $9-30\%$ (depending on the classification method) posses an AGN. To identify AGNs in our samples of void galaxies we use the standard flux ratios log([OIII]/Hβ) and log([NII]/Hα) as suggested by Baldwin, Philips, & Telervich (1981, BPT) and Villieux & Osterbrock (1987). The galaxy's position on this plot of log([OIII]/Hβ) versus log([NII]/Hα) indicates whether it is an AGN or star-forming galaxy.

From our sample of void galaxies we only select those galaxies for all four lines have been measured in order to compute the respective ratios. Following the approach of K03a we then plot our void galaxies on the BPT diagram and look for galaxies that have $\log([\mathrm{NII}]/\mathrm{H}\alpha) > -0.2$ and $\log([\mathrm{OIII}]/\mathrm{H}\beta) > 0.5$ simultaneously. This yields 20 void galaxies (out of 760 with $> 3\sigma$ detections) that have AGNs with high confidence (i.e. Seyferts). As suggested by Miller et al. (2003) an AGN can also be detected by only looking at a high log([OIII]/Hβ) or log([NII]/Hα) ratios. Therefore, if we simply look for a high log([NII]/Hα) (> -0.2) ratio, our sample of AGNs increases from 20 to 65 i.e., about 9% of our void galaxies have an AGN compared to 15% in the wall galaxies (1055/7151 with $> 3\sigma$ detections). In Figure 3 we plot the BPT diagram for the distant sample of void galaxies. Filled circles in the top right corner are the 'high confidence' AGNs (Seyferts) ($\log([\mathrm{NII}]/\mathrm{H}\alpha) > -0.2$ and $\log([\mathrm{OIII}]/\mathrm{H}\beta) > 0.5$) and galaxies that have $\log([\mathrm{NII}]/\mathrm{H}\alpha) > -0.2$ (top right and bottom right corners) are the additional AGNs (these include the Seyferts and Liners). The solid curve is the modified Kewley et al. (2001) demarcation curve from K03a:

$$\log([\mathrm{OIII}]/\mathrm{H}\beta) > \frac{0.61}{\log([\mathrm{NII}]/\mathrm{H}\alpha) - 0.05} + 1.3 \tag{16}$$

Any galaxy that lies above this curve is classified as an AGN and any galaxy that lies below it is

a star-forming galaxy. With this criterion, we find that 234 void galaxies are classified as having an AGN (i.e. 31%) in contrast to 35% in the wall galaxy sample (2494/7151). In the nearby samples we find a lower fraction of AGNs, at most 10% from the nearby void galaxies and 17% from the nearby wall galaxies. Further examination of their equivalent widths confirms that we have identified AGNs based on their broad emission lines as can be seen in Figure 5. In this paper we do not discuss the individual properties of AGNs in voids and leave this as a topic for future research.

7. Conclusions

Acknowledgments

Funding for the creation and distribution of the SDSS Archive has been provided by the Alfred P. Sloan Foundation, the Participating Institutions, the National Aeronautics and Space Administration, the National Science Foundation, the U.S. Department of Energy, the Japanese Monbukagakusho, and the Max Planck Society. The SDSS Web site is http://www.sdss.org/.

The SDSS is managed by the Astrophysical Research Consortium (ARC) for the Participating Institutions. The Participating Institutions are The University of Chicago, Fermilab, the Institute for Advanced Study, the Japan Participation Group, The Johns Hopkins University, Los Alamos National Laboratory, the Max-Planck-Institute for Astronomy (MPIA), the Max-Planck-Institute for Astrophysics (MPA), New Mexico State University, University of Pittsburgh, Princeton University, the United States Naval Observatory, and the University of Washington.

MSV acknowledges support from NSF grant AST-0071201 and a grant from the John Templeton Foundation. We acknowledge David Goldberg for useful conversations and the referee's valuable comments in helping us make the paper clearer.

REFERENCES

Abazajian, K., et al. 2003, ApJ submitted, astro-ph/0305492

Alonso, M. V., da Costa, L., Latham, D., Pellegrini, P. S., & Milone, A. E. 1994, AJ, 108, 1987

Babul, A., & Postman, M. 1990, ApJ, 359, 280

Baldry, I. K., et al. 2003, ApJ submitted, astro-ph/0309710

Benson, A. J., Hoyle, F., Torres, F., & Vogeley, M. S. 2003, MNRAS, 340, 160

Bingelli, B., Tammann, G. A., & Sandage, A. 1987, AJ, 94, 251

Bingelli, B. 1989, Large scale structure and motions in the universe; Proceedings of the International Meeting, Trieste, Italy, Apr. 6-9, 1988

Blanton, M. R., Lin, H., Lupton, R. H., Maley, F. M., Young, N., Zehavi, I., & Loveday, J. 2003, AJ, 125, 2276

Blanton, M. R., et al. 2003, AJ, 125, 2348

Blanton, M. R., et al. 2002, ApJ, 594, 186

de Lapparent, V., Geller, M. J., & Huchra, J.P. 1991, ApJ, 369, 273

Bremnes, T., Bingelli, B., & Prugniel, P. 1998, A&AS, 129, 313

Caldwell, N., & Bothun, G. D. 1987,AJ, 94, 1126

da Costa, L. N., et al. 1998, AJ, 116, 1

Dekel, A., & Silk, J. 1986, ApJ, 303, 39

Dressler, A. 1980, ApJ, 236, 351

Efstathiou, G., Ellis, R. S., & Peterson, B. S. 1988, MNRAS, 233, 431

Eisenstein, D. J., et al. 2001, AJ, 122, 2267

El-Ad, H., & Piran, T. 1997, ApJ, 491, 421

El-Ad, H., Piran, T., & da Costa, L. N. 1996, ApJ, 462, 13

El-Ad H., Piran, T., & da Costa, L. N. 1997, MNRAS, 287, 790

Falco, E. E., et al. 1999, PASP, 111, 438

Frenk, C. S., et al. 2000, astro-ph/0007362

Fukugita, M., Shimasaku, K., Ichikawa, T. 1995, PASP, 107, 945

Fukugita, M., Ichikawa, T., Gunn, J. E., Doi, M., Shimasaku, K., & Schneider, D. P. 1996, AJ, 111, 1748

Grogin, N. A., & Geller, M. J. 1999, ApJ, 118, 2561

Grogin, N. A., & Geller, M. J. 2000, ApJ, 119, 32

Gunn, J. E., et al. 1998, ApJ, 116, 3040

Geller, M. J., & Huchra, J. P. 1989, Science, 246, 857

Hoffman, Y., Silk, J., & Wyse, R. F. G. 1992, ApJ, 388, L13

Hogg, D. W., Finkbeiner, D. P., Schlegel, D. J., & Gunn, J. E. 2001, AJ, 122, 2129

Hogg, D. W., et al. 2002, ApJ, 124, 646

Hogg, D. W., et al. 2002, ApJ submitted, astro-ph/0212085

Hoyle, F. & Vogeley, M. S. 2002, ApJ, 566, 641

Huchra, J. P., Geller, M. J., de Lapparent, V., & Corwin, H. 1990, ApJS, 72, 433

Huchra, J. P., Geller, M. J., & Corwin, H. 1995, ApJS, 99, 391

Huchra, J. P., Vogeley, M. S., & Geller, M. J. 1999, ApJS, 121, 287

Jerjen, H., Binggeli, B., & Freeman, K. C. 2000, AJ, 119, 593

Karachentsev, I. D., & Makarov, D. A. 1996, ApJ, 111, 794

Kirshner, R. P., Oemler, A. Jr., Schechter, P. L., Shectman, S. A. 1981, ApJ, 248, 57

Kniazev, A. Y. et al. 2003, in preparation

Kuhn, B., Hopp, U., & Elaässer, H. 1997, A&A, 318, 405

Lanzetta, K. M., Bowen, D. V., Tytler, D., & Webb, J. K. 1995, ApJ, 442, 538

Lupton, R. H., Gunn, J. E., Ivezić, Ž., Knapp, G. R., Kent, S., & Yasuda, N. 2001, in ASP Conf. Ser. 238, Astronomical Data Analysis Software and Systems X, ed. F. R. Harnden, Jr., F. A. Primini & H. E. Payne (San Francisco: ASP), 269

Lupton, R. H., et al. 2002, in preparation

McLin, K. M., Stocke, J. T., Weymann, R. J., Penton, S. V., Shull, J. M. 2002, ApJ, 574, 115

Mo, H. J., McGaugh, S. S., & Bothun, G. D. 1994, MNRAS, 267, 129

Morris, A. L., Weymann, R. J., Dressler, A., McCarthy, P. J., Smith, B. A., Terrile, R. J., Giovanelli, R., & Irwin, M. 1993, ApJ, 419, 524

Müller, V., Arbabi-Bidgoli, S., Einasto, J., Tucker, D. 2000, MNRAS, 318, 280

Park, C., Vogeley, S. M., Geller, M. J., & Huchra, J. P. 1994, ApJ, 431, 569

Peebles, P. J. E. 2001, ApJ, 557, 495

Pellegrini, P. S., da Costa, L. N., & de Carvalho, R. R. 1989, ApJ, 339, 595

Pence, W. 1976, ApJ, 203, 39

Pier, J. R., Munn, J. A., Hindsley, R. B., Hennessy, G. S., Kent, S. M., Lupton, R. H., & Ivezić, Ž. 2003, AJ, 125, 1559

Plionis, M., & Basilakos, S. 2002, MNRAS, 330, 399

Popescu, C., Hopp, U., & Elaässer, H. 1997, A&A, 325, 881

Postman, M., & Geller, M. J. 1984, ApJ, 281, 95

Pustilnik, S. A., Martin, J. -M., Huchtmeier, W. K., Brosch, N., Lipovetsky, V. A., Richter, G. M. 2002, A&AS 389, 405

Schlegel, D. J., Finkbeiner, D. P., & Davis, M. 1998, ApJ, 500, 525

Sandage, A., & Binggeli, B. 1984, AJ, 89, 919

Scranton, R. et al. 2002, ApJS, 579, 48

Sersic J. L. 1968, Atlas de Galaxias Australes. Observatorio Astronómico, Cordoba.

Shectman, S. A., et al. 1996, ApJ, 470, 172

Shimasaku, K., et al. 2001, AJ, 122, 1238

Smith, J. A., et al. 2002, AJ, 123, 2121

Staveley-Smith, L., Davies, R., & Kinman, T. D. 1992, MNRAS, 258, 334

Stoughton, C. et al. 2002, AJ, 123, 485

Strauss, M. A., et al. 2002, AJ, 124, 1810S

Strateva, I., et al. 2001, ApJ, 122, 1874

Sung, E., Han C., Ryden, B. S., Chun, M., Kim, H. 1998, ApJ, 499, 140

Tegmark, M., Hamilton, A. J. S., & Xu, Y. 2002, MNRAS, 335, 887

Thuan, T. X., Gott, J. R. III, & Schneider, S. E. 1987, ApJ, 315, L93

Vader, J.P., Vigroux, L., Lachieze-Rey, M., & Souviron, J. 1988, A&A, 203, 217

Vennik, J., Hopp, U., Kovachev, B., Kuhn, B., & Elsässer, H. 1996, A&AS, 117, 261

York, D. G. et al. 2000, AJ, 120, 1579

Zwicky, F., Herzog, E., & Wild, P. 1961, Catalogue of galaxies and clusters of galaxies, (Pasadena: California Institute of Technology) Vol. I

Zwicky, F., & Herzog, E. 1962-1965, Catalogue of galaxies and clusters of galaxies, (Pasadena: California Institute of Technology) Vol. II-IV

Zwicky, F., Karpowicz, M., & Kowal, C. 1965, Catalogue of galaxies and clusters of galaxies, (Pasadena: California Institute of Technology) Vol. V

Zwicky, F., & Kowal, C. 1968, Catalogue of galaxies and clusters of galaxies, (Pasadena: California Institute of Technology) Vol. VI

SDSS VOID GALAXY CATALOG

Void Galaxy Catalog Format

Column	Parameter	Format	Description
1.	RA	F8.4	J2000 Right Ascension [degrees]
2.	DEC	F8.4	2000 Declination [degrees]
3.	z	F8.4	Redshift
4.	RUN	I4	Run number of this object
5.	RERUN	I4	Rerun number of this object
6.	CAMCOL	I1	Camera column number of this object
7.	FIELD	I4	Field number of this object
8.	OBJID	I6	Object number of this object
9.	PLATE	I5	Plate for this object
10.	FIBERID	I4	Fiber ID
11.	MJD	I5	Last 5 digits of the modified Julian date
12.	M_u	F8.3	SDSS u-band absolute magnitude
13.	M_g	F8.3	SDSS g-band absolute magnitude
14.	M_r	F8.3	SDSS r-band absolute magnitude
15.	M_i	F8.3	SDSS i-band absolute magnitude
16.	M_z	F8.3	SDSS z-band absolute magnitude
17.	CI	F8.3	Concentration index
18.	n	F8.3	Sersic Index
19.	Ha_SIGMA	F8.4	Sigma of the fitted Gaussian [Å]
20.	Ha_SIGMA_ERR	F8.4	Error in the width of the fitted Gaussian [Å]
21.	Ha_HEIGHT	F8.4	Height of the fitted Gaussian [10^{-17}ergs s^{-1} cm^{-2} Å^{-1}]
22.	Ha_HEIGHT_ERR	F8.4	Error on the height of the fitted Gaussian [10^{-17}ergs s^{-1} cm^{-2} Å^{-1}]
23.	Ha_EW	F8.4	Equivalent width [Å]
24.	Ha_EW_ERR	F8.4	Error on the equivalent width [Å]
25.	Ha_CONT	F8.4	Continuum value at this pixel [10^{-17}ergs s^{-1} cm^{-2} Å^{-1}]
26.	Hb_SIGMA	F8.4	Sigma of the fitted Gaussian [Å]
27.	Hb_SIGMA_ERR	F8.4	Error in the width of the fitted Gaussian [Å]
28.	Hb_HEIGHT	F8.4	Height of the fitted Gaussian [10^{-17}ergs s^{-1} cm^{-2} Å^{-1}]
29.	Hb_HEIGHT_ERR	F8.4	Error on the height of the fitted Gaussian [10^{-17}ergs s^{-1} cm^{-2} Å^{-1}]
30.	Hb_EW	F8.4	Equivalent width [Å]
31.	Hb_EW_ERR	F8.4	Error on the equivalent width [Å]
32.	Hb_CONT	F8.4	Continuum value at this pixel [10^{-17}ergs s^{-1} cm^{-2} Å^{-1}]
33.	OII_SIGMA	F8.4	Sigma of the fitted Gaussian [Å]
34.	OII_SIGMA_ERR	F8.4	Error in the width of the fitted Gaussian [Å]
35.	OII_HEIGHT	F8.4	Height of the fitted Gaussian [10^{-17}ergs s^{-1} cm^{-2} Å^{-1}]
36.	OII_HEIGHT_ERR	F8.4	Error on the height of the fitted Gaussian [10^{-17}ergs s^{-1} cm^{-2} Å^{-1}]
37.	OII_EW	F8.4	Equivalent width [Å]
38.	OII_EW_ERR	F8.4	Error on the equivalent width [Å]
39.	OII_CONT	F8.4	Continuum value at this pixel [10^{-17}ergs s^{-1} cm^{-2} Å^{-1}]
40.	NII_SIGMA	F8.4	Sigma of the fitted Gaussian [Å]
41.	NII_SIGMA_ERR	F8.4	Error in the width of the fitted Gaussian [Å]
42.	NII_HEIGHT	F8.4	Height of the fitted Gaussian [10^{-17}ergs s^{-1} cm^{-2} Å^{-1}]
43.	NII_HEIGHT_ERR	F8.4	Error on the height of the fitted Gaussian [10^{-17}ergs s^{-1} cm^{-2} Å^{-1}]
44.	NII_EW	F8.4	Equivalent width [Å]
45.	NII_EW_ERR	F8.4	Error on the equivalent width [Å]
46.	NII_CONT	F8.4	Continuum value at this pixel [10^{-17}ergs s^{-1} cm^{-2} Å^{-1}]
47.	OIII_SIGMA	F8.4	Sigma of the fitted Gaussian [Å]
48.	OIII_SIGMA_ERR	F8.4	Error in the width of the fitted Gaussian [Å]
49.	OIII_HEIGHT	F8.4	Height of the fitted Gaussian [10^{-17}ergs s^{-1} cm^{-2} Å^{-1}]
50.	OIII_HEIGHT_ERR	F8.4	Error on the height of the fitted Gaussian [10^{-17}ergs s^{-1} cm^{-2} Å^{-1}]
51.	OIII_EW	F8.4	Equivalent width [Å]
52.	OIII_EW_ERR	F8.4	Error on the equivalent width [Å]
53.	G_SYNTH	F8.3	Synthetic magnitude in G
54.	R_SYNTH	F8.3	Synthetic magnitude in R
55.	SFR(Ha)	F8.4	Hα derived star formation rate [$M_\odot$ yr^{-1}]
56.	MASS	F8.4	Stellar mass [$\log_{10} M/M_\odot$] from K03a and and a least square fit
57.	S-SFR(Ha)	F8.4	Hα derived star formation rate per unit stellar mass [yr^{-1}]
58.	D4000	F8.4	Strength of the 4000 Å Balmer break from K03a
59. - 63.	Di_nn	F8.3	Distance to the i^{th} nearest neighbor [h^{-1}Mpc] for $i = 1 - 5$ using an $(\Omega_m, \Omega_\Lambda) = (0.3, 0.7)$ cosmology

Table 1:

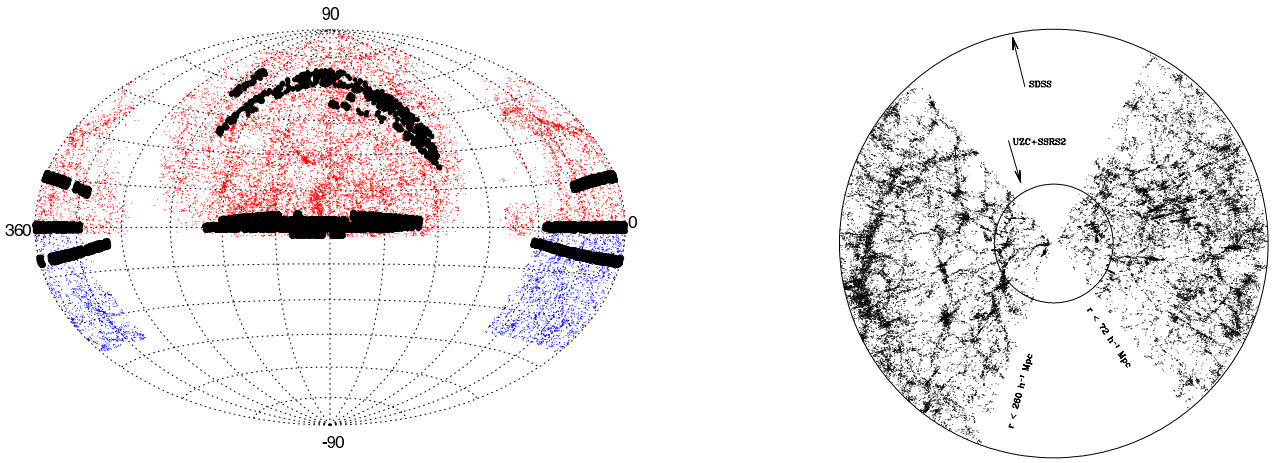

Fig. 1.— The left plot shows an Aitoff projection in celestial coordinates of the current SDSS galaxy redshift survey data (black points) and the combined Updated Zwicky Catalog and Southern Sky Redshift Survey (gray dots). Approximate coordinates of each region are given in the text in Section 2. The right plot shows a cone diagram of the flux-limited SDSS data with $|\delta| \lesssim 15°$. The inner circle is drawn at $72h^{-1}$Mpc, which is the depth of the combined UZC and SSRS2 volume-limited sample. The outer circle is drawn at $260h^{-1}$Mpc, which is the depth of the SDSS volume-limited sample. In the region $100 < r < 260h^{-1}$Mpc we use the SDSS data to trace the distribution of the voids. However, nearby the SDSS currently is limited in volume as only narrow strips have been observed. Therefore, nearby we use the UZC+SSRS2 to trace the voids out to $72h^{-1}$Mpc.

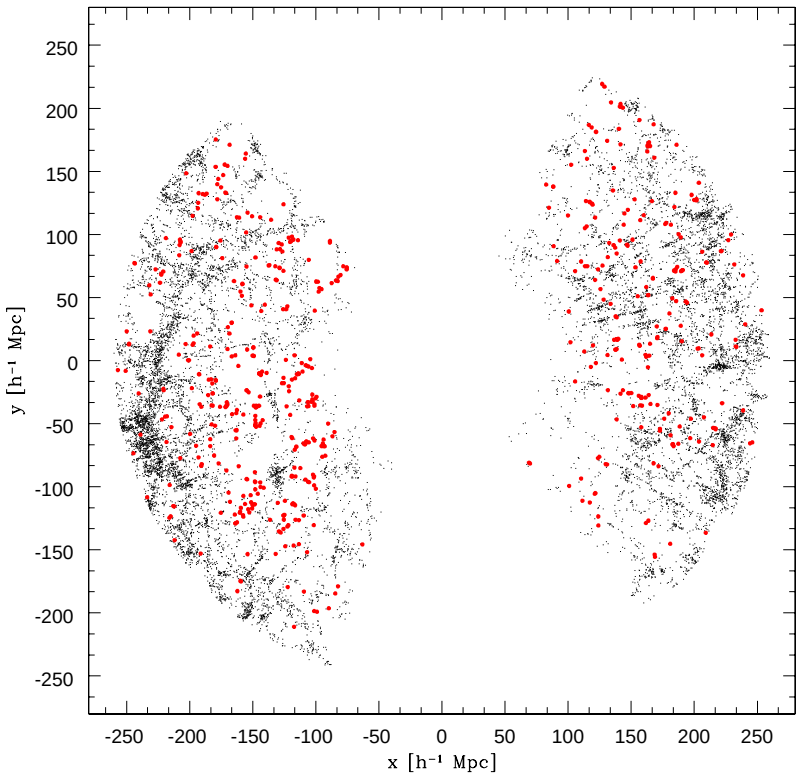

Fig. 2.— Redshift space distribution of void and volume-limited galaxies. The gray dots show a cone diagram of the SDSS volume-limited SDSS galaxies ($100 < r < 260h^{-1}$Mpc, $M_r \lesssim -17.5$). The black points show the void galaxies from the apparent magnitude-limited sample ($r < 17.5$). We only plot galaxies with $|\delta| \lesssim 15°$. Note that some of the black points appear to be close to volume-limited galaxies. This is, however, just a projection effect (we suppress the z direction) and all void galaxies have less than three neighbors within a 3-dimensional radius of $7h^{-1}$Mpc.

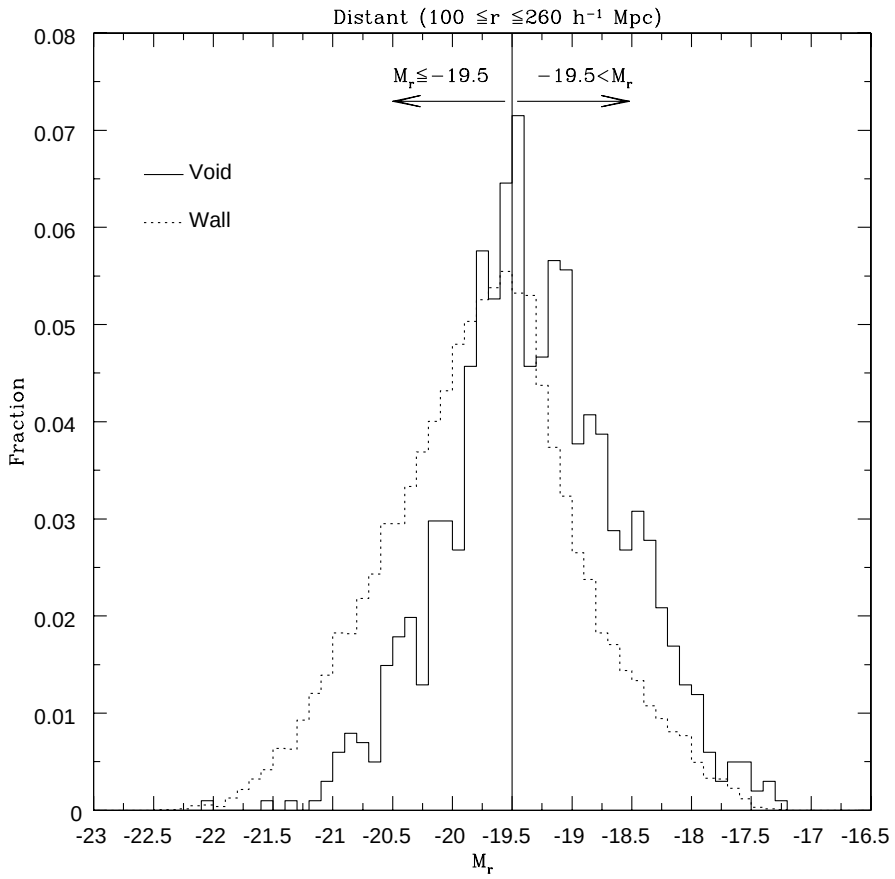

Fig. 3.— Distribution of the absolute magnitudes in the distant wall (WGD, dotted line) and void (VGD, solid line) galaxy samples. The parent sample is apparent magnitude-limited at $r \leq 17.5$ and redshift limited at $z \leq 0.089$. We split both data sets at $M_r = -19.5$ to obtain the void galaxy sub-samples [VGD_b (b=bright), VGD_f (f=faint)] and wall galaxy sub-samples [WGD_b, WGD_f]. The cut at $M_r = -19.5$ divides both the void and wall galaxy samples into approximately equal halves. This histogram bins galaxies by $\Delta M = 0.1$. The range of absolute magnitudes probed by the void galaxies that lie within this volume is $-22.0 \lesssim M_r \lesssim -17.2$.

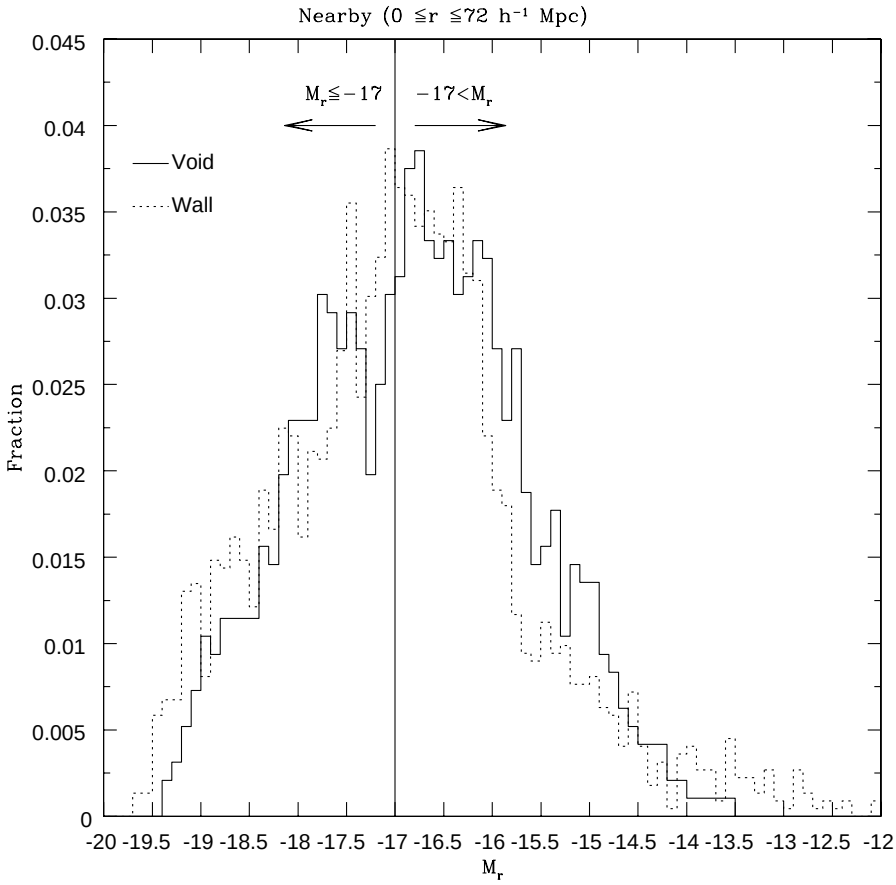

Fig. 4.— Distributions of absolute magnitudes in the nearby wall (WGN, dotted line) and void (VGN, solid line) galaxy samples. The parent sample is apparent magnitude-limited at $r \leq 17.5$ and redshift limited at $z \leq 0.025$. Both data sets are split at $M_r = -17$ to obtain the void galaxy sub-samples [VGN_b (b=bright), VGN_f (f=faint)] and wall galaxy sub-samples [WGN_b, WGN_f]. The cut at $M_r = -17$ divides both the void and wall samples into approximately equal halves. This histogram bins galaxies by $\Delta M = 0.1$. The range of absolute magnitudes probed by the void galaxies that lie within this volume is $-19.7 \lesssim M_r \lesssim -13.0$.